THE ASTROPHYSICAL JOURNAL, 466:585–594, 1996 July 20

PIXON-BASED MULTIRESOLUTION IMAGE RECONSTRUCTION FOR *YOHKOH*'S HARD X-RAY TELESCOPE

THOMAS R. METCALF AND HUGH S. HUDSON
Institute for Astronomy, University of Hawaii, 2680 Woodlawn Drive, Honolulu, HI 96822
TAKEO KOSUGI
National Astronomical Observatory of Japan, 2-1-1 Osawa, Mitaka, Tokyo 181 Japan
AND
R. C. PUETTER AND R. K. PIÑA
Center for Astrophysics and Space Sciences, University of California, San Diego, 9500 Gilman Drive, La Jolla, CA 92093-0111
Received 1995 September 12; accepted 1996 February 2

ABSTRACT

We present results from the application of pixon-based multiresolution image reconstruction to real and simulated data from *Yohkoh's* Hard X-ray Telescope (HXT). The goal of the pixon algorithm is to minimize the number of degrees of freedom used to describe an image within the accuracy allowed by the noise. This leads to a reconstruction that is optimally constrained. We apply the pixon code to two solar flares in the HXT database and compare the results of the pixon reconstruction to the results of a direct, linear, smoothed inversion of the HXT Fourier synthesis data and to a maximum entropy reconstruction. The maximum entropy reconstruction is vastly better than the direct inversion, but the pixon reconstruction gives superior noise suppression and photometry. Further, the pixon reconstruction does not suffer from overresolution of the images.

Subject headings: methods: numerical — Sun: flares — Sun: X-rays, gamma rays — techniques: image processing

1. INTRODUCTION

The most successful modern methods of image reconstruction are nonlinear. Linear methods, such as Fourier deconvolution, are more compact and less computationally demanding, but they have poor noise propagation properties. Nonlinear methods are more complex but allow some control over the propagation of the noise. Indeed, maximum entropy methods (MEMs) have been quite successful in controlling the noise propagation in image reconstruction.

Bayesian image reconstruction algorithms, which include ME and pixon methods, use a statistical approach to obtain the most likely image given the constraints of the data. The likelihood of an image is defined by two terms: first, the goodness of fit (GOF), which characterizes how well the image and image model predict the data, and, second, the image prior, which characterizes the a priori probability of the image and model, without regard to the data. As discussed in § 2, different image priors distinguish between the various Bayesian reconstruction algorithms. In MEMs, the image prior states that the flattest image is a priori the most likely image. In pixon-based methods, the image prior states that the image with the fewest degrees of freedom is most likely.

For hard X-ray imaging using the bi-grid modulation collimators of the hard X-ray telescope (HXT; Kosugi et al. 1991) on board the *Yohkoh* spacecraft, the reconstruction problem is particularly difficult. The HXT data set is sparse, consisting of only 64 collimator outputs from which a relatively large image (typically 64 × 64) is normally reconstructed. Pixon-based reconstruction is ideally suited to this problem since the goal of the method is to minimize the number of degrees of freedom and hence to make the best possible use of the limited data. While an ME method has been successfully applied to HXT solar flare data by Sakao (1994), we do not expect a hard X-ray image of a solar flare to be flat. Hence, pixon-based methods should provide a significant improvement.

Below, we review the theory of pixon-based image reconstruction and describe a pixon-based algorithm used to reconstruct hard X-ray images for HXT. Finally, we apply the algorithm to two solar flare data sets and compare the results to an ME reconstruction and to a direct, linear inversion of the Fourier data.

2. PIXON-BASED IMAGE RECONSTRUCTION

Most nonlinear image reconstruction methods can be understood in terms of a Bayesian estimation scheme in which the reconstructed image is, in some sense, the most probable (e.g., Puetter 1995a). This implies maximizing the joint probability distribution of the reconstructed image (I) and the model (M) given the data (D): $p(I, M \mid D)$. The model defines the relationship between the data and the image (e.g., the physics of the image encoding process, the pixel size, etc.). Using Bayes' theorem, this probability distribution can be factored to yield

$$p(I, M \mid D) = \frac{p(D \mid I, M)p(I \mid M)p(M)}{p(D)} \propto p(D \mid I, M)p(I \mid M) , \quad (1)$$

where $p(X \mid Y)$ is the probability of X given Y. Here we use $p(I, M \mid D)$ rather than $p(I \mid D, M)$ since the model is allowed to vary in the pixon method.

The terms on the far right side of equation (1) are easily interpreted. The term $p(D \mid I, M)$ is simply the GOF, measuring the likelihood of the data given the image and model. Typically, $p(D \mid I, M)$ is set to $\exp(-\chi^2/2)$. The second term, $p(I \mid M)$, is called the image prior since it does not depend on the data and can be calculated a priori before taking data.

The choice of the image prior distinguishes the various nonlinear reconstruction algorithms. For example, in maximum entropy (ME), the prior is taken to be exp (αS), where S is the entropy of the image. This implies, a priori, that the flattest image is the most probable. Thus, when maximizing $p(I \mid D, M)$, MEMs attempt to find the flattest image that is statistically consistent with the data.[1] In GOF or maximum likelihood image reconstruction, $p(I \mid M)$ is assumed to be constant and the algorithm finds the best fit to the data (and the noise) alone.

The key idea behind pixon-based image reconstruction is the realization that not all parts of an image require the same spatial resolution. Indeed, for hard X-ray imaging of solar flares, discussed below, most of the image is blank and has no information content.[2] Why then should blank pixels be included as additional degrees of freedom? To avoid this, Piña & Puetter (1993) introduced the concept of a pixon.

A pixon is a generalized pixel. It is a variable cell in the image representing a single degree of freedom in the reconstruction. Ideally, the set of pixons used to describe the image would be the minimum set required to describe the information content of the image. The pixon shapes, sizes, and positions would follow the information density, with the smallest pixons where the information content is the highest. Having reduced the reconstruction to the fewest possible degrees of freedom, it makes the best possible use of the available data.

An image prior that favors this reduction in the number of degrees of freedom is based on simple counting arguments (Puetter 1995a):

$$p(I \mid M) = \frac{N!}{n^N \prod_i N_i!}, \tag{2}$$

where n is the number of cells (pixons), $\{N_i\}$ denotes the number of events (counts) in cells i, and $N = \sum_i N_i$. In the pixon method, n, N_i, and the sizes and positions of the cells are variable parameters that are to be determined by the data. Since equation (2) must be maximized, the goal of the pixon algorithm is to find the fewest number of cells that pack as much information into each cell as possible, while still satisfying the GOF criterion.

Here we see that the pixon method is an extension of the MEM. Indeed, using Stirling's approximation to the factorial, equation (2) is maximized when the entropy *in the pixon basis* is maximized:

$$\frac{N!}{n^N \prod_i N_i!} \approx \frac{1}{n^N} \exp\left(-\sum_i \frac{N_i}{N} \ln \frac{N_i}{N}\right). \tag{3}$$

Hence, a pixon-based reconstruction is a ME reconstruction in which the image model and prior are allowed to vary in an optimal way.

With the prior given by equation (3), the image reconstruction reduces to a calculation of the pixon parameters (number, size, position, and intensity) that maximize

$$p(I, M \mid D) \propto \frac{1}{n^N} \exp\left[-\left(\frac{\chi^2}{2} + \sum_i \frac{N_i}{N} \ln \frac{N_i}{N}\right)\right]. \tag{4}$$

While it is possible to maximize equation (4) with a multidimensional search algorithm, Puetter (1995a) suggests a more efficient iterative procedure that does not implement equation (4) directly. With an initial guess for the image ($\{N_i\}$) and model (pixon number, size, and position), the reconstruction proceeds by first calculating the best image with the model held fixed, then calculating an improved model holding the image fixed, and iterating to convergence.

Puetter & Piña (1993) introduced the fractal pixon basis (FPB) as a practical implementation of the pixon concept. In this "fuzzy" pixon basis, the pixons do not have hard edges; adjacent pixons share some of each other's signal. The reconstructed image is represented as the local convolution of a pseudoimage with a pixon shape function, which varies over the image:

$$I(\boldsymbol{x}_i) = \int_{V_y} dV_y K_i\left(\frac{\boldsymbol{y} - \boldsymbol{x}_i}{\delta_i}\right) I_{\text{pseudo}}(\boldsymbol{y}). \tag{5}$$

Here, x_i is the location of pixel i, $I(\boldsymbol{x})$ is the reconstructed image, K_i is the pixon shape function used at pixel i and

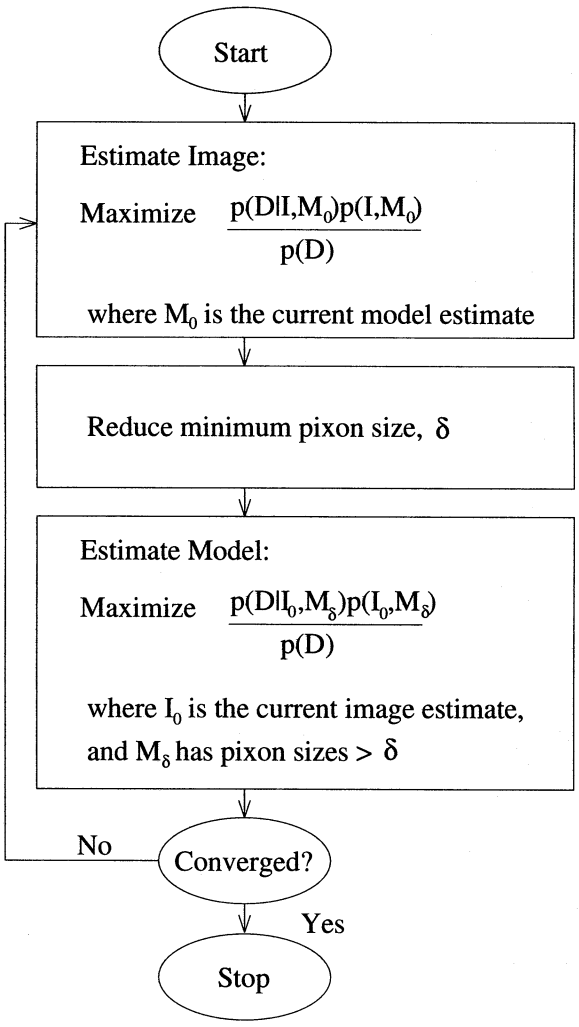

FIG. 1.—A schematic diagram of the iterative scheme used for the HXT pixon-based image reconstructions. To estimate the image, we iterate the pseudoimage until the posterior probability of the image, using the current model estimate, is maximized. To estimate the model, we compute the pixon map, which maximizes the posterior probability of the model, using the current image estimate, i.e., the pixon map with the fewest possible number of pixons. Adapted from Puetter (1995a).

[1] "Flat" is used in a global sense here since MEMs generally do not consider correlations between adjacent pixels.

[2] The contrast of the hard X-ray brightness distribution is extremely large. The background, due to stray diffuse hard X-ray fluxes and cosmic-ray effects, can be assumed to have no imaginable structure.

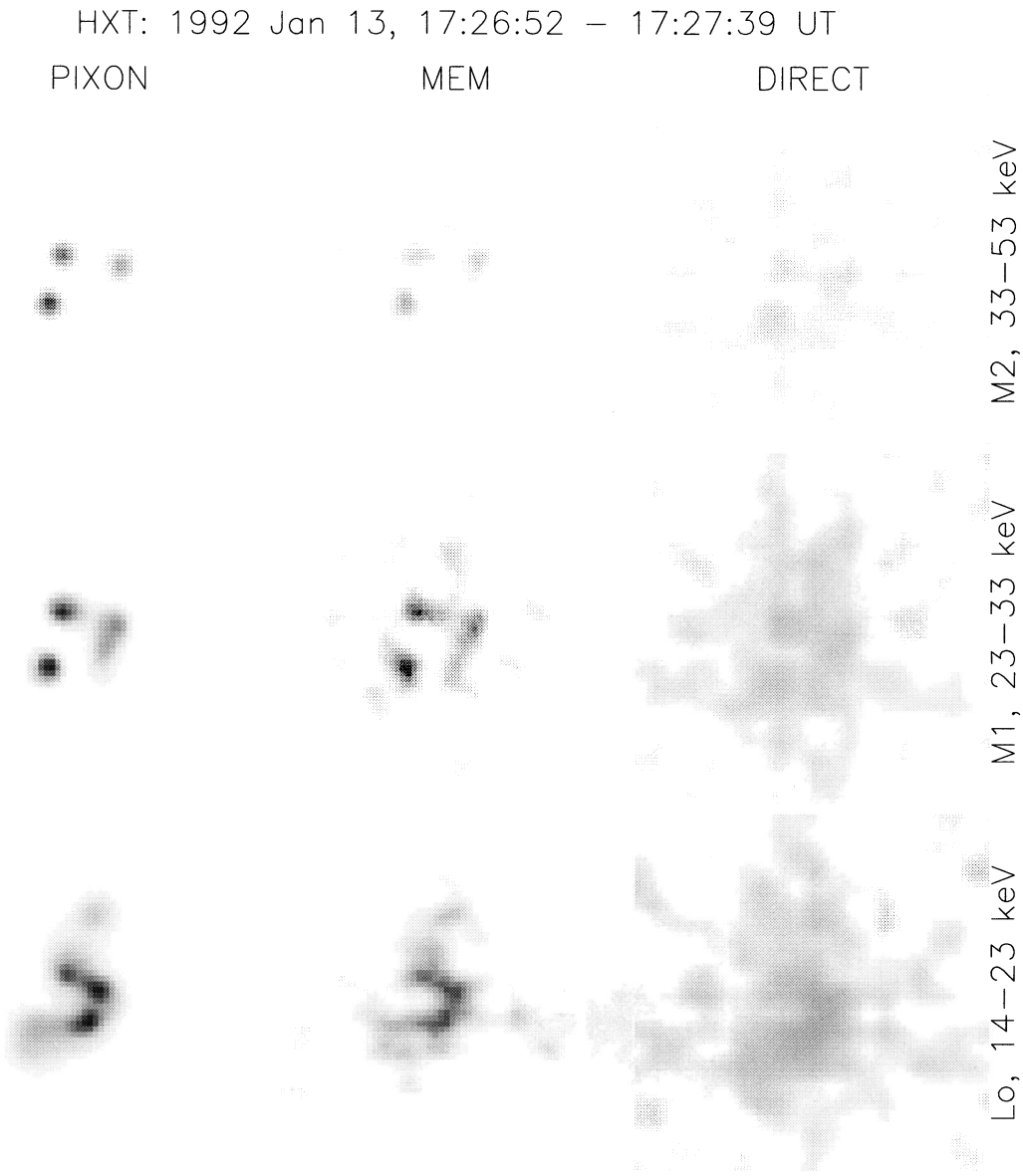

FIG. 2.—A comparison of three image reconstruction algorithms applied to three HXT energy bands in the solar flare of 1992 January 13 (17:26:52–17:27:39 UT). The first column shows the pixon-based image reconstruction while the second and third columns show an ME reconstruction and a direct, smoothed inversion of the data, respectively. All images are negative images and use the same gray scale. The images are oriented with solar north up and solar east to the left. Each image is 64 × 64 with 2".46 pixels.

normalized such that

$$\int_{V_y} dV_y K_i\left(\frac{y}{\delta_i}\right) = 1 , \tag{6}$$

δ_i is the pixon size at pixel i (the pixon map), $I_{\text{pseudo}}(y)$ is the pseudoimage, and the integration is over the volume in y-space, i.e., over the pseudoimage. The goal of the FPB algorithm is to find the pseudoimage and pixon map which, together, yield the reconstructed image that maximizes equation (4). Hence, the pseudoimage is simply an intermediary that allows a straightforward implementation of the spatial correlations required for the pixon algorithm; once the calculation is complete the pseudoimage is discarded. In the fuzzy pixon scheme, the number of pixons (the number of degrees of freedom) is computed as (Puetter & Piña 1995)

$$n = \sum_i \frac{1}{\int_{V_y} dV_y k_i(y/\delta_i)} , \tag{7}$$

where k_i is the pixon shape function normalized to 1 at $y = 0$.

The spatial correlations introduced through the smoothing functions restrict the number of degrees of freedom in the reconstruction. The pixon problem then becomes calculation of the pixon map, the map of the shape function size, and functional form at each pixel. In principle, this is accomplished by testing each shape function and size at every pixel and maximizing the evidence for the model: $p(M \mid D) \propto p(D \mid I_0, M)p(I_0 \mid M)$ (Puetter 1995a), where I_0 is the current image estimate. In practice, equation (4) tells us to find the set of cells that minimizes the number of pixons but is still consistent with the data, i.e., find the spatially largest smoothing function consistent with the data at every pixel.

Typically, the pixon shape functions are taken to be a finite set of normalized, circularly symmetric functions. The functions chosen define the pixon basis. This choice is a trade-off between the desire to have a very rich set of basis

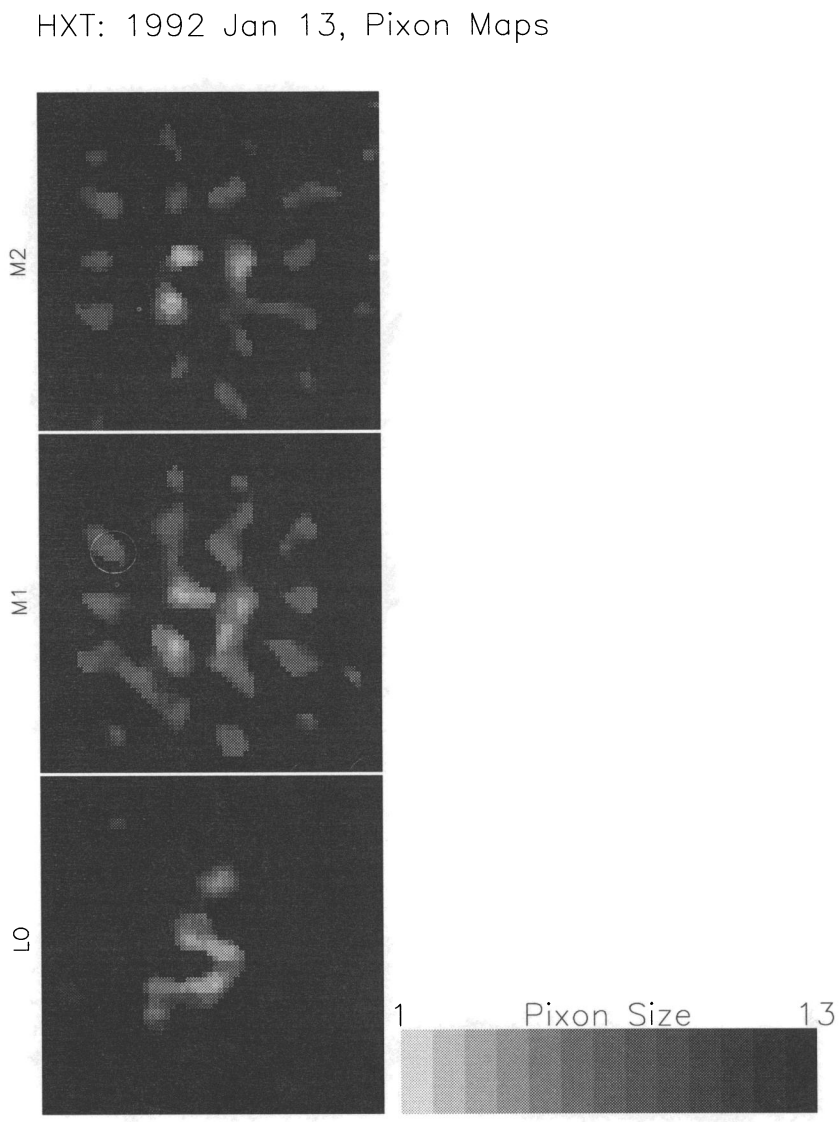

FIG. 3.—The pixon maps for the 1992 January 13 pixon image reconstructions. The scale shows the spatial resolution required by the data.

functions and the need to restrict the computational demands of the reconstruction. For example, with the HXT data presented below, we use a normalized, circularly symmetric, truncated paraboloid as the only shape function, with δ_i in the set $\{1, 2, \ldots, 13\}$ pixels.

Once the pixon map is determined, the algorithm iteratively adjusts the pseudoimage until the reconstructed image, from equation (5), maximizes equation (4). This maximization is equivalent to minimizing $\chi^2 + 2\sum_i (N_i/N)\ln(N_i/N)$, provided that we use the fewest possible number of pixons so that the $1/n^N$ term is also maximized. However, in the fuzzy pixon basis, the $\{N_i\}$ are not well defined since the pixons do not have hard boundaries. In this case we set

$$2\sum_{\text{pixons}} \frac{N_i}{N}\ln\frac{N_i}{N} = 2\sum_{\text{pixels}} \frac{N_i}{N}\ln\frac{N_i/f_i}{N}, \tag{8}$$

where pixel i is a fraction f_i of a pixon:

$$f_i = \frac{1}{\int_{V_y} dV_y\, k_i(y/\delta_i)}. \tag{9}$$

In practice, the entropy term is not important in the pixon method. The reduction in the number of degrees of freedom forces the GOF term in equation (4) to be very sharply peaked and the ME prior is essentially constant over the peak. Hence, we can approximate the entropy term by

$$2\sum_{\text{pixons}} \frac{N_i}{N}\ln\frac{N_i}{N} \approx 2\alpha\sum_{\text{pixels}} \frac{N_i}{N}\ln\frac{N_i}{N}, \tag{10}$$

where the sum over pixons is approximated by a sum over pixels by setting

$$\alpha \equiv \frac{\ln n}{\ln n_{\text{pixels}}}. \tag{11}$$

Here, n_{pixels} is the number of pixels and n is the number of pixons. In equation (11), α is the ratio of the image entropy over all pixons to the image entropy over all pixels, in the special case when all pixels and pixons have uniform brightness, i.e., in the case when the entropy is maximized. This is an upper limit to the true α, which is in the range $0 \le \alpha \le (\ln n)/(\ln n_{\text{pixels}}) \le 1$.

TABLE 1

RECONSTRUCTION OF SIMULATED DATA[a]

Location	True	Pixon	MEM
Test 1			
South footpoint (maximum counts per pixel)	30.0	27.1	7.4
North footpoint (maximum counts per pixel)	30.0	25.4	9.7
South footpoint (total counts)	119.8	119.5	58.4
North footpoint (total counts)	119.8	134.4	80.7
Looptop (maximum counts per pixel)	5.9	12.4	7.1
Looptop (total counts)	142.8	138.9	78.8
Entire image (total counts)	587.2	590.8	601.6
Test 2			
South footpoint (maximum counts per pixel)	45.0	42.8	22.5
North footpoint (maximum counts per pixel)	45.0	43.0	23.6
South footpoint (total counts)	179.8	175.2	145.4
North footpoint (total counts)	179.8	173.5	144.0
Looptop (maximum counts per pixel)	5.9	5.4	1.9
Looptop (total counts)	142.8	78.7	64.2
Entire image (total counts)	707.2	700.0	672.6
Test 3			
South footpoint (maximum counts per pixel)	179.9	142.0	124.1
North footpoint (maximum counts per pixel)	179.9	139.6	136.6
South footpoint (total counts)	719.8	637.7	646.7
North footpoint (total counts)	719.8	699.7	650.3
Looptop (maximum counts per pixel)	5.9	0.2	2.6
Looptop (total counts)	142.8	12.2	47.1
Entire image (total counts)	1787.2	1787.1	1742.7

[a] Counts above background.

3. A PIXON ALGORITHM FOR FOURIER SYNTHESIS HARD X-RAY IMAGING

The Hard X-Ray Telescope on board the *Yohkoh* spacecraft uses a set of 64 bi-grid modulation collimators to image the Sun in energies between 13.9 and 92.8 keV in four energy bands. Each subcollimator is a pair of nearly identical one-dimensional grids mounted in parallel planes separated by 1.4 m (Kosugi et al. 1991). The 64 grid pairs have differing pitch and orientation to approximately measure the Fourier components of the image. Fourier synthesis imaging is necessary since there is no effective way to manufacture optics that focus hard X-ray radiation. The HXT data set consists of the count rate of hard X-ray radiation observed through each subcollimator:

$$d_j = \int_{V_y} dV_y I(\mathbf{y}) P_j(\mathbf{y}) , \quad 0 \le j < 64 , \tag{12}$$

where d_j is the count rate observed in subcollimator j, $I(\mathbf{y})$ is the image to be reconstructed, $P_j(\mathbf{y})$ is the modulation pattern for subcollimator j, computed from the known characteristics of the subcollimator (Sakao 1994), and $\mathbf{y}$ is a vector representing the location of the image elements (pixels). The image must be reconstructed from these 64 data points and modulation patterns.

This is a difficult problem since the data are sparse. The finest grids on HXT have an angular repetition period of 16″, and the synthesis aperture is nominally 134″. Hence, a 16 × 16 image array with 256 elements would be the minimum required to double-sample the finest resolutions. The normal reconstruction is onto a 64 × 64 array of standard 2.″46 pixels that covers a somewhat larger field of view. The standard *Yohkoh*/HXT imaging software has been the maximum entropy method of Gull & Daniell (1978) and Willingale (1981), in the implementation described by Sakao (1994). However, with 4096 degress of freedom (dof) but only 64 data points, spurious sources are expected. Since the pixon-based image reconstruction minimizes the number of degrees of freedom, it will give superior results. For HXT data sets, we typically find at most 100 dof sufficient for pixon image reconstruction. Hence, spurious sources are greatly reduced or eliminated.

A related advantage of the pixon-based reconstruction is better photometry. The number of counts observed in the field of view is approximately conserved regardless of the algorithm used in the reconstruction (e.g., Metcalf et al. 1990, footnote 4). Hence, if there are spurious sources, these counts are removed from the real sources yielding poor photometry. Thus, a pixon-based reconstruction that eliminates spurious sources will have better photometry than other methods.

The key to FPB image reconstruction is the pixon map (Puetter 1995a). The pixon map gives the local spatial scale of the image at each pixel and, hence, determines the size and location of the pixons required to reconstruct the image. We require that the pixon map be computed in such a way that equation (4) is maximized; i.e., we require that, within the chosen pixon basis, the algorithm find the fewest number of pixons, each with the largest signal-to-noise ratio, that are consistent with the data. To guarantee this, and hence to guarantee that the pixon map is uniquely determined by the data, we compute the large-scale structure in the image before computing the small-scale structure. This is done by iterating to a solution with the pixons forced to be large, i.e., by using only the largest pixon smoothing functions. We then reiterate the image and pixon map, while slowly lowering the size of the smallest allowed pixon. This ensures that, at each pixel, we apply the largest

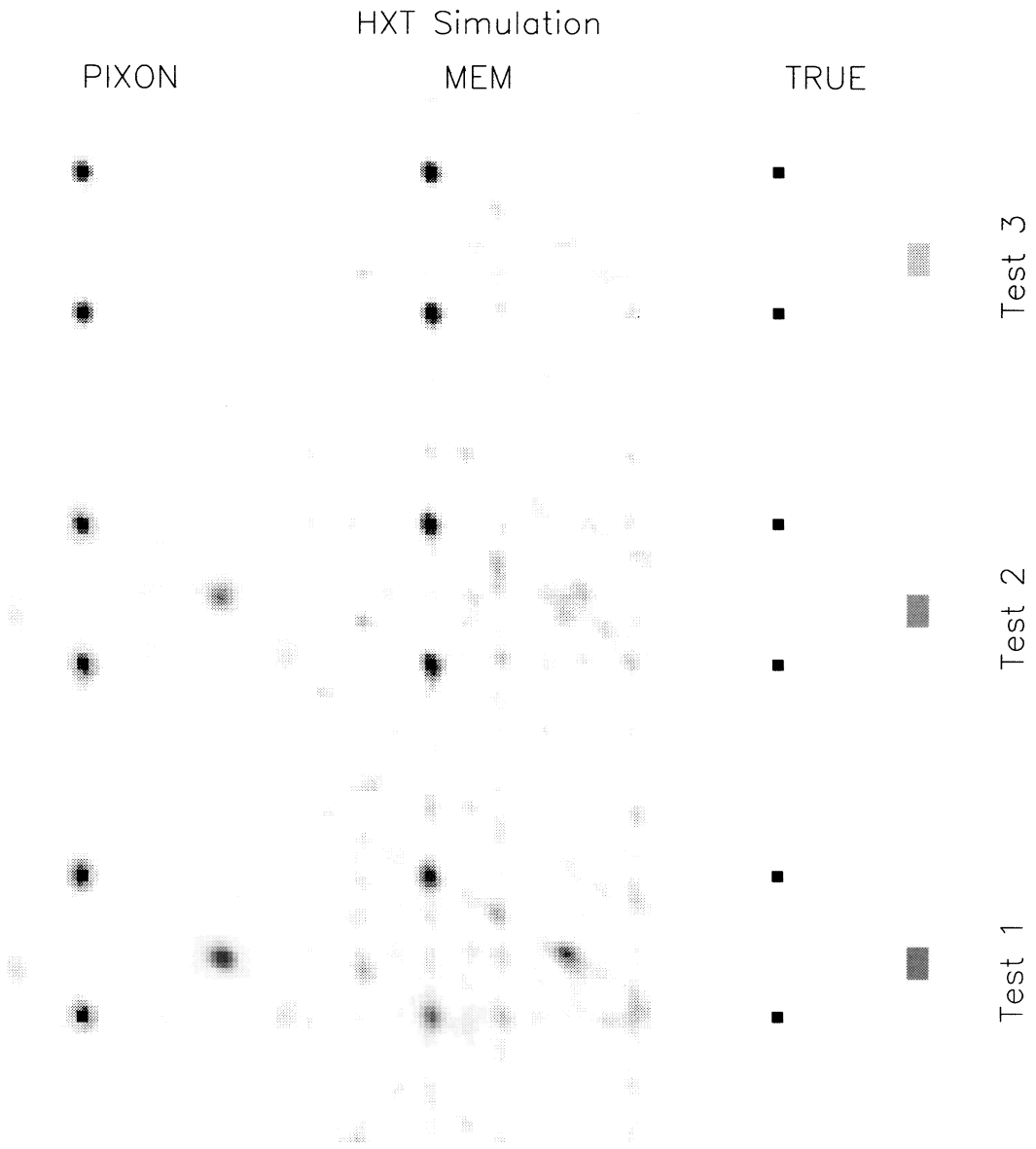

FIG. 4.—Reconstructions of simulated HXT data using both the pixon and the MEM algorithms. The images are similar to the 1992 January 13 flare. From test 1 to test 3, the extended source grows fainter relative to the compact sources. In test 1, the compact emission is 5 times brighter that the extended emission. In tests 2 and 3, the compact emission is 7.5 and 30 times brighter than the extended emission, respectively. Each image is 64 × 64 with 2".46 pixels.

pixon shape function allowed by the data. Hence, the pixons are as large as possible and the image is never overresolved, an important advantage over ME.

As the smallest allowed pixon size is lowered, we independently test each pixel at the new resolution to compute a new pixon map. We examine, pixel by pixel, the variation in the GOF parameter (G) given by

$$\delta G(s_i) \equiv \delta s_i \frac{\partial G}{\partial s_i} \tag{13}$$

to test whether a smaller pixon shape function is justified by the data. Here, s is the size of the pixon shape function and i is the pixel number; the calculation of $\partial G/\partial s_i$ is discussed in the Appendix. When the pixon size at a particular pixel is reduced, the number of degrees of freedom in the reconstruction increases. If the new, smaller pixon size is valid, we expect the magnitude of the decrease in χ^2, used as the GOF parameter in the HXT reconstructions, to be at least as large as the increase in the number of degrees of freedom.[3] If this is not the case, the new pixon size is not supported by the data and the larger scale is retained. Each pixel is tested independently; the pixon map is not updated until every pixel has been tested at the new resolution.

Once the new pixon map is determined, we iteratively solve for the reconstructed image using conjugate gradient minimization; the pixon map is held fixed during the iteration. Although the reconstructed image is used to compute χ^2, the FPB algorithm iterates the pseudoimage, not the

[3] Since the expectation of χ_i^2 is the number of degrees of freedom in pixel i, f_i, we require $-\Delta\chi_i^2 > \Delta f_i$ (e.g., Press et al. 1992, pp. 695–698). For robustness, one can consider the width of the χ^2 distribution, $(2f_i)^{1/2}$ and require $-\Delta\chi_i^2 > \Delta f_i[1 + \sigma/(2f_i)^{1/2}]$, where σ is a constant of order 1. With $\sigma = 1$, the pixon map is computed at the 68% confidence level, etc.

reconstructed image. The details are shown in the Appendix.

The conjugate gradient minimization of $\chi^2 + 2\alpha \sum_i (N_i/N) \ln (N_i/N)$ is completed for each value of the smallest allowed pixon size before the value is lowered. For the HXT data, we start by iterating on a 64 × 64 reconstruction grid with the pixon size set to 13 pixels everywhere in the image. We then reduce the smallest allowed pixon size by 1 pixel, recompute the pixon map with the image held fixed, and finally reiterate the image with the new pixon map held fixed. This procedure is repeated until we have cycled through all the allowed resolutions. Figure 1 shows a schematic diagram of the iterative scheme used for the FPB reconstruction.

To be fully consistent with equation (4), the ME prior from equation (10) is included in the conjugate gradient minimization when iterating the image intensity. However, since the number of degrees of freedom in the HXT reconstruction is drastically reduced by the use of pixons, the GOF term in equation (1) is sharply peaked and the prior is essentially uniform over this peak. Hence, in most cases the ME prior is not necessary. For HXT data, we have tried the iteration both ways, and inclusion of the ME term does not affect the reconstructed image significantly. However, in the examples shown in the next section, we include the ME term for full consistency with the theory presented above.

Due to the convolutions required for implementation, fuzzy pixons are inefficient. Instead of utilizing only the n independent image elements, the fuzzy pixon algorithm utilizes every pixel in the image. For the HXT data, a pixon algorithm that used only the 100 or so independent pixons would be far more efficient in terms of computational resources. This is a clear direction for future research. Another direction for future research is to study the effect of different pixon shape functions. For example, shape functions with an elliptical rather than circular footprint have been successfully used for other astronomical data sets (Puetter 1995b).

4. RESULTS

Masuda et al. (1994) studied hard and soft X-ray images of a flare that occurred near the west solar limb on 1992 January 13. Since this important event is well known, and since it has an interesting combination of diffuse and unresolved emission in the 14–23, 23–33, and 33–55 keV HXT channels (LO, M1, and M2 channels, respectively), we chose it for a detailed comparison of the pixon-based, ME, and direct image reconstruction algorithms. In the higher energy channels, the flare was characterized by a pair of compact sources to the east (footpoint emission) and a faint, extended source to the west (loop top emission). Puetter (1995a) showed a similar comparison for a compact flare observed on the solar disk on 1992 August 20. Here, we make a more in-depth comparison, showing the details of the pixon-based image reconstruction.

Figure 2 compares image reconstructions for the 1992 January 13 solar flare. Each column shows a different reconstruction algorithm while each row shows a different HXT energy channel; all images have a common gray-scale representation. Comparing the images across the three rows, the advantages of the pixon algorithm are clear: the pixon reconstructions show less background structure and, hence, are brighter, implying better photometry. Further, the ME images seem to be overresolved. They have smaller scale structure than the pixon images, but the χ^2 value for the ME and pixon reconstructions are nearly identical. Hence, the ME resolution is unjustified.

Figure 3 shows the pixon maps for the image reconstructions shown in the first column of Figure 2 and details the spatial resolution required by the data. Clearly, in the M1 and M2 channels, there is structure in the pixon maps that is not required to produce the images shown in Figure 2. This may be the result of an uncertainty in the noise level due to an inaccurate calibration of the modulation patterns. More accurate modulation patterns should give a pixon map that matches the image, much like the LO channel in Figures 2 and 3. In the January 13 event, the signal-to-noise ratio in the LO channel is significantly higher than in the M1 and M2 channels, and hence the LO channel pixon map is cleaner. In the absence of better modulation patterns, setting $\sigma \approx 1$ in the pixon map $\Delta\chi^2$ test (eq. [13] and footnote 3) results in cleaner pixon maps. This does not significantly affect the reconstructed images, however, since even the "dirty" pixon maps greatly constrain the reconstruction.

To further test the reconstruction algorithms, we simulated emission similar to the January 13 flare and generated HXT data, which we then used to reconstruct images. The results are shown in Figure 4 for three different test cases. The simulated data consist of a uniform background with two bright footpoint sources (compact, 4 pixels) and a faint loop top source (diffuse, 24 pixels) superimposed. Further, Gaussian noise with a standard deviation equal to the square root of the count rate in each subcollimator is added. The faint loop top source grows fainter relative to the footpoint emission from test 1 through test 3. When computing the simulated HXT data, we assumed that the modulation patterns for HXT are perfectly known and used the same collimator phases for all three tests.

In each test, the total number of counts in each reconstructed image is approximately the same, regardless of the reconstruction algorithm. Hence the primary difference between the reconstructions is the spatial location of the counts. In each MEM reconstruction, the emission is spread out into spurious background structures, causing the brightness of the footpoint emission to be reduced. The pixon algorithm suppresses the spurious sources and hence has better photometry, particularly for the bright sources (Table 1). In test 3, neither the pixon nor the MEM algorithm detected the faint loop top source. In this case, the faint source should be below the threshold of the HXT instrument (the footpoint emission is 30 times brighter than the loop top emission, comparable to the noise from photon counting statistics). The pixon algorithm, however, does a better job of suppressing the spurious sources in test 3, where the loop top source is not significant.

As a final demonstration of the pixon algorithm, Figure 5 shows an FPB image reconstruction for the solar limb flare of 1992 February 21 (Tsuneta et al. 1992). This was a gradual event with weak but long-enduring hard X-ray emission. The underlying image in Figure 5 is from the Soft X-ray Telescope (SXT) on *Yohkoh* (Tsuneta et al. 1991) using the Be filter, and the contours are from the FPB reconstruction of the LO channel on HXT. The SXT-Be and HXT-LO data are primarily thermal in origin and are sensitive to similar plasma temperatures, so we expect a

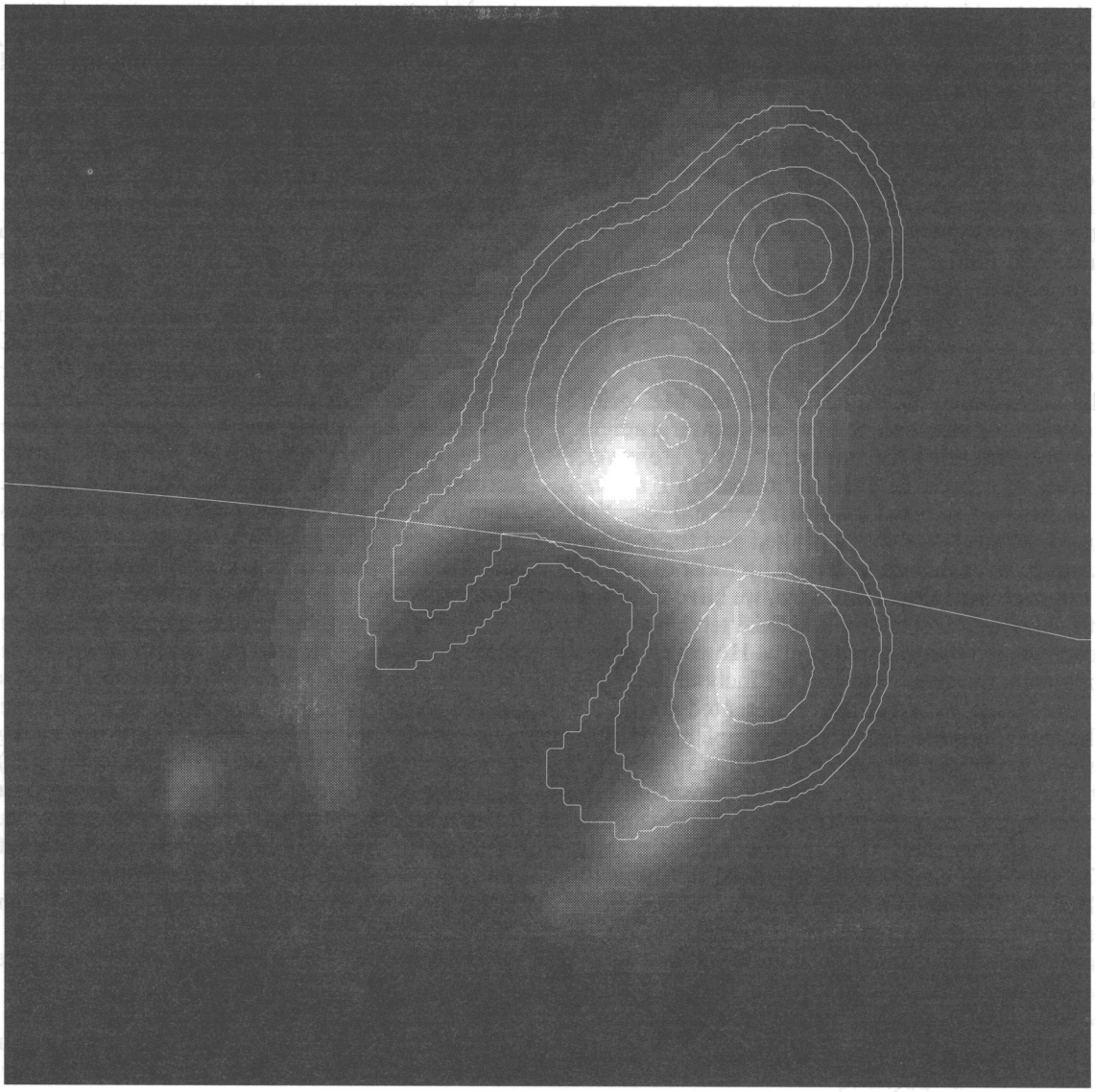

FIG. 5.—HXT LO channel contours overlaid on an SXT image for the 1992 February 21 limb flare. The HXT contours are at 0.06, 0.08, 0.15, 0.25, 0.4, 0.65, and 0.95 of the maximum value. The SXT image, obtained at 03:20:14 UT, uses the beryllium filter. The HXT data was summed from 03:15:00 through 03:25:04. The image is 64 × 64 with 2".46 pixels. Solar east is up, and solar north is to the right. The curved line passing through the image shows the location of the solar limb.

good (but not perfect) correspondence between the two images. The pixon-based reconstruction adequately reproduces the expected image. In this case, small pixons were not justified since the signal-to-background ratio was quite low; it is apparent from the HXT contours that the pixons are large (8 pixels). For this 1992 February 21 data set, the ME reconstruction has not yet been successful in producing a meaningful image.

5. CONCLUSIONS

We have demonstrated the application of multiresolution pixon image reconstruction to solar flare data from *Yohkoh's* Hard X-ray Telescope. The comparison of the pixon reconstruction with the direct, smoothed, linear inversion of the HXT Fourier synthesis data and with the MEM demonstrates the desirable characteristics of the pixon-based reconstruction. Although the ME reconstruction is vastly superior to the direct inversion, the pixon reconstruction gives superior noise suppression and photometry. Further, the pixon reconstruction does not suffer from overresolution of the images. As expected on theoretical grounds, the pixon reconstruction provides superior images for HXT data.

The research at the University of Hawaii was supported through Lockheed under NASA contract NAS 8-37334 with the Marshall Space Flight Center. R. C. P. and R. K. P. acknowledge support from the NSF, NASA, and the California Association for Research in Astronomy.

APPENDIX A

CALCULATION OF THE χ^2 DERIVATIVES

The derivative of the GOF parameter, χ^2, and the ME prior with respect to the pseudoimage at every pixel ($\partial\chi^2/\partial I_i^{(P)}$, etc.) is required for the conjugate gradient iteration while $\partial\chi^2/\partial s$ is required to compute the pixon map.[4] Here, $I_i^{(P)}$ is the pseudoimage at pixel i. For the HXT Fourier synthesis data, we compute $d\chi^2/dI_i^{(P)}$ as follows:

$$\frac{\partial}{\partial I_i^{(P)}}\chi^2 = \frac{\partial}{\partial I_i^{(P)}}\sum_j \frac{R_j^2}{\sigma_j^2} = 2\sum_j \frac{R_j}{\sigma_j^2}\frac{\partial R_j}{\partial I_i^{(P)}}, \tag{A1}$$

where R_j is the residual in the jth data point, σ_j is the error estimate for the jth data point, and $\partial/\partial I_i^{(P)}$ represents a variation in count rate in the ith pseudoimage pixel holding the pixon map fixed. The error estimate, σ_j, has two parts: the square root of the observed counts and a systematic term related to the poor calibration of the HXT modulation patterns. The residual is given by

$$R_j = \left(\sum_k I_k P_{jk}\right) - d_j, \tag{A2}$$

where I_k is the count rate in the kth image pixel (not pseudoimage pixel), P_{jk} is the set of modulation patterns computed for the HXT subcollimators (Sakao 1994), and d_j is the jth data point. Since $\partial P_{jk}/\partial I_i^{(P)}$ and $\partial d_j/\partial I_i^{(P)}$ are zero, we have

$$\frac{\partial R_j}{\partial I_i^{(P)}} = \sum_k \frac{\partial I_k}{\partial I_i^{(P)}} P_{jk}. \tag{A3}$$

In a maximum likelihood or ME algorithm, $\partial I_k/\partial I_i^{(P)}$ would simply be δ_{ki}, the Kronecker delta; however, for the fuzzy pixon basis, a change in $I_i^{(P)}$ will affect many of the surrounding pixels, depending on the size of the pixon. Hence, $\partial I_k/\partial I_i^{(P)}$ is K_{ki}, the magnitude of the ith pixon shape function at pixel k. Thus,

$$\frac{\partial R_j}{\partial I_i^{(P)}} = \sum_k K_{ki} P_{jk}, \tag{A4}$$

which is simply the modulation patterns convolved with the pixon shape functions, i.e., the modulation patterns in the current pixon basis. In practice, we introduce a positivity constraint on the reconstructed image by iterating to the logarithm of the pseudoimage. In this case, we compute

$$\frac{\partial}{\partial(\ln I_i^{(P)})}\chi^2 = 2\sum_j \frac{R_j}{\sigma_j^2}\frac{\partial R_j}{\partial(\ln I_i^{(P)})}, \tag{A5}$$

where

$$\frac{\partial R_j}{\partial(\ln I_i^{(P)})} = \sum_k K_{ki} P_{jk} I_k^{(P)}. \tag{A6}$$

Using similar reasoning, we find, for the derivatives of the ME prior,

$$\frac{\partial}{\partial I_i^{(P)}} 2\alpha \sum_k \frac{I_k}{I_{\text{total}}} \ln\frac{I_k}{I_{\text{total}}} = \frac{2\alpha}{I_{\text{total}}}\sum_k K_{ki}\left(1 + \ln\frac{I_k}{I_{\text{total}}}\right), \tag{A7}$$

and

$$\frac{\partial}{\partial \ln I_i^{(P)}} 2\alpha \sum_k \frac{I_k}{I_{\text{total}}} \ln\frac{I_k}{I_{\text{total}}} = \frac{2\alpha}{I_{\text{total}}}\sum_k K_{ki}\left(1 + \ln\frac{I_k}{I_{\text{total}}}\right) I_k^{(P)}. \tag{A8}$$

For the derivative of χ^2 with respect to the pixon size, we have

$$\frac{\partial\chi^2}{\partial s_i} = I_i^{(P)} \sum_j \frac{2R_j}{\sigma_j^2}\sum_k \frac{\Delta K_{ik}}{\delta s} P_{jk}. \tag{A9}$$

Here, I_{total} is $\sum_i I_i$ (assumed constant), ΔK_{ik} is the difference between the pixon smoothing function centered at pixel i, but evaluated at pixel k, for two resolutions, and δs is the difference in resolution for the two shape functions used in ΔK_{ik}.

[4] For Poisson statistics, replace $2R_j/\sigma_j^2$ by $\ln(D_j/d_j)$ in eqs. (A1), (A5), and (A9), where $D_j = \sum_k I_k P_{jk}$.

REFERENCES

Gull, S. F., & Daniell, G. J. 1978, Nature, 272, 686
Kosugi, T., et al. 1991, Sol. Phys., 136, 17
Masuda, S., Kosugi, T., Hara, H., Tsuneta, S., & Ogawara, Y. 1994, Nature, 371, 495
Metcalf, T. R., Canfield, R. C., Avrett, E. H., & Metcalf, F. T. 1990, ApJ, 350, 463
Piña, R. K., & Puetter, R. C. 1993, PASP, 105, 630.
Press, W. H., Teukolsky, S. A. Vetterling, W. T., & Flannery. B. P. 1992, Numerical Recipes in C (2d ed.; Cambridge: Cambridge Univ. Press)
Puetter, R. C. 1995a, Int. J. Image Systems Technol., 6, 314
———. 1995b, private communication
Puetter, R. C., & Piña, R. K. 1995, in Proc. MaxEnt93 Conf., Santa Barbara, in press
Sakao, T. 1994, Ph.D. thesis, Univ. of Tokyo
Tsuneta, S., et al. 1991, Sol. Phys., 136, 37
———. 1992, PASJ, 44, L63
Willingale, R. 1981, MNRAS, 194, 359